SIMULATION OF FLOW AND TRANSPORT PROCESSES IN A DISCRETE FRACTURE-MATRIX SYSTEM II. EFFICIENT AND ACCURATE STREAMLINE APPROACH

H. HÆGLAND, A. ASSTEERAWATT, R. HELMIG, AND H. K. DAHLE

Abstract. Simulations of flow and transport in fractured porous rocks using a discrete fracture model have gradually become more practical, as a consequence of increased computer power and improved simulation and characterization techniques. Fractures in a discrete model are generally described with one dimension less than the surrounding matrix, the so-called lower-dimensional approach. However, high numerical diffusion in the transport simulation causes an increased computational demand due to the fine-grid requirement. A streamline method for transport for a lower dimensional discrete fracture model (DFML) is proposed in this paper. By solving the mass conservation equation using a vertex-centered finite volume scheme, a pressure field is obtained. Then, a fracture expansion and a flux recovery method are carried out to determine new mass conservative fluxes on a hybrid grid of triangles and quadrilaterals, on which streamlines are traced. Only the advective transport is assumed for the streamline method. The results of the streamline method are compared with a grid-based finite volume method using two different fracture-matrix systems: simple systems (a single fracture or systematically distributed fractures) and complex fracture-matrix systems. Significantly different transport behavior can be observed in the two types of systems. The numerical diffusion in the grid-based transport simulation smears out the heterogeneity effect (fast transport in the fractures and slow transport in the matrix) and delays the plume migration. Whereas, the purely advective transport without numerical diffusion in the streamline method leads to faster transport.

1. Introduction

Simulations of flow and transport in fractured porous rocks using a discrete fracture model have gradually become more practical, as a consequence of increased computer power and improved simulation and characterization techniques. In a discrete fracture model, fractures may either be discretized with the same dimension as the surrounding matrix elements, the so-called equi-dimensional approach, or with one dimension less than the matrix, the so-called lower-dimensional approach. The comparison study of the two discretization approaches presented in Neunhäuserer [19] revealed a number of local differences for the flow and transport, but and only minor differences globally. Sufficient accuracy of global solutions with reduction of the computational time have lead to wide-spread application of the lower-dimensional approach, see e.g., [23, 17, 14, 16], and references therein.

In advective dominated problems like transport in fracture-matrix systems, grid-based methods such as finite difference, finite element and finite volume methods all using the Eulerian approach, suffer from numerical diffusion. High numerical diffusion in the transport simulation, as shown in the associated paper, gives rise to an increased computational burden since a very fine grid is required. Streamline methods have become a viable alternative to traditional finite element or finite difference reservoir simulation during the last decade ([15, 27]). The advantages of streamline simulation are lower computational demand and less numerical diffusion compared with a grid-based transport model. On

the reservoir scale where fractures and matrix are treated as two interacting continua, promising results from streamline tracing have been presented by Huang et al. [12] and Al-Huthali and Datta-Gupta [1]. Their results showed a close agreement with the results from a grid-based finite difference simulation with a significant reduction in run time. In this work, we propose a streamline method for transport for the lower dimensional discrete fracture model (DFML). Similar to the grid-based methods, the streamline method is based on the velocity field determined from a flow simulation.

The precision of streamline tracing strongly depends on the accuracy of the velocity field ([18]). For finite element based solutions, approximating the velocity from pressure gradients results in discontinuous fluxes at element boundaries and hence lack of mass conservation ([8]). Many papers have considered this problem recently, see e.g. [7, 5, 26], and references therein. Cordes and Kinzelbach [6] proposed an inexpensive technique for deriving a continuous distribution of fluxes from the finite element solutions. The method solves a local problem for each grid node to obtain conservative fluxes in a patch surrounding the node. This technique was extended by Prévost et al. [22] for the control-volume finite element scheme on unstructured grids. A flux continuous velocity for a sub cell of a control volume (triangular or quadrilateral in 2D, and tetrahedron or hexahedron in 3D) were reconstructed. In this work, a flux recovery for a two-dimensional fracture-matrix system based on the work of Cordes and Kinzelbach [6] and Prévost et al. [22] is introduced. Continuous and mass conservative fluxes for all sub cells of a control volume denoted as sub control-volumes are recorded and are later used for streamline tracing. Additionally, when streamline tracing is considered, lower-dimensional fractures, which are assumed in the flow simulation have to be extended to equi-dimensional fractures to obtain well-defined velocities in the fractures.

Due to the post processing and the use of unstructured grids, streamline tracing for general quadrilateral grids are required. For a regular quadrilateral mesh (rectangular mesh), Pollock's method [20] has been widely used. The extension of Pollock's method to unstructured grids has been presented in several studies. Cordes and Kinzelbach [6] extended Pollock's method to linear and bilinear finite element methods for groundwater flow, and later Prévost et al. [22] extended it for streamline tracing with the control volume finite element method, flux continuous scheme and the multipoint flux approximation (MPFA) method.

The objective of this paper is to present a streamline method for a lower dimensional discrete fracture model (DFML). In the next section, the streamline method is presented stepwise. First, the governing equation and numerical discretization for the flow process are summarized. Second, the flux recovery together with fracture expansion are described. Later, the streamline tracing using Pollock's method on unstructured grids and the evaluation of the breakthrough curve from the time-of-flight are introduced. Finally, the results obtained from the streamline method and from the grid-based finite volume method are compared.

2. Streamline Method

2.1. **Solution of the flow equation.** The continuity equation for an incompressible fluid in a nondeformable matrix is given as

$$\nabla \cdot \boldsymbol{q} = 0 \,, \tag{1}$$

where $\boldsymbol{q}$ is the Darcy velocity. Combining Equation (1) with Darcy's law and neglecting the gravitational effect yields

$$\nabla \cdot \boldsymbol{q} = -\nabla \cdot \frac{\boldsymbol{K}}{\mu} \nabla p = 0 \,, \tag{2}$$

where $\boldsymbol{K}$ is the permeability, μ is the dynamic viscosity and p is the pressure, [4].
A vertex-centered finite volume method, also called box method, is used in this study since it can be applied to unstructured grids of a fracture-matrix system and is locally mass conservative ([23]). The spatial discretization of the box method, described in more detail in Hægland et al. [10], is based on a primary finite element (FE) mesh and a secondary finite volume (FV) mesh. First, the domain is discretized into a FE mesh, where matrix properties are assumed to be constant on each element. Next, by connecting element barycenters with edge midpoints, a FV mesh is constructed, see Figure 1. With each vertex of the FV mesh there is an associated control volume. Each control volume consists of a set of sub cells denoted sub control-volumes as illustrated in Figure 1. Fractures are described by a one-dimensional line in a two-dimensional domain with an associated virtual width equal to their aperture, the so-called lower-dimensional approach ([23]).

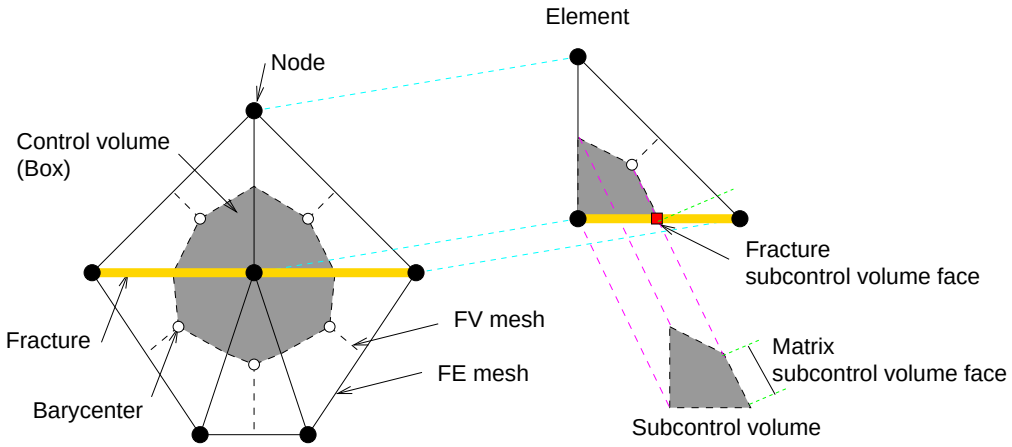

FIGURE 1. Finite Element (FE) and Finite Volume (FV) mesh.

The pressure is assumed to vary linearly within each element, and fluxes are evaluated using Darcy's law at the exterior boundary of a control volume. denoted as sub control-volume faces (see Figure 1). After the linear system of equations for the pressure field has been solved, conservative fluxes over all control volume faces can be determined. Note that fluxes are in general discontinuous at element boundaries, but they are continuous at the control volume boundaries.

2.2. **Flux recovery.** The precision of streamline tracing strongly depends on the accuracy of the velocity field. Approximating the velocity field using pressure gradients from the flow simulation results in discontinuous fluxes at element boundaries, not only when the permeabilities of neighboring elements are different but also when they are the same ([25]). On the basis of Cordes and Kinzelbach [6] and Prévost et al. [22], a flux recovery for a two-dimensional fracture-matrix system is introduced in this work to obtain continuous fluxes on a sub-quadrilateral grid. Additionally, lower-dimensional fractures, which are assumed in the flow simulation, have to be extended to equi-dimensional fractures to obtain well-defined velocities in the fractures (not only parallel to the fractures orientation), see [10].

Fractures are expanded such that the resulting 2D fractures have a width equal to the associated fracture aperture d and the 1D fracture is the center line, see Figure 2.

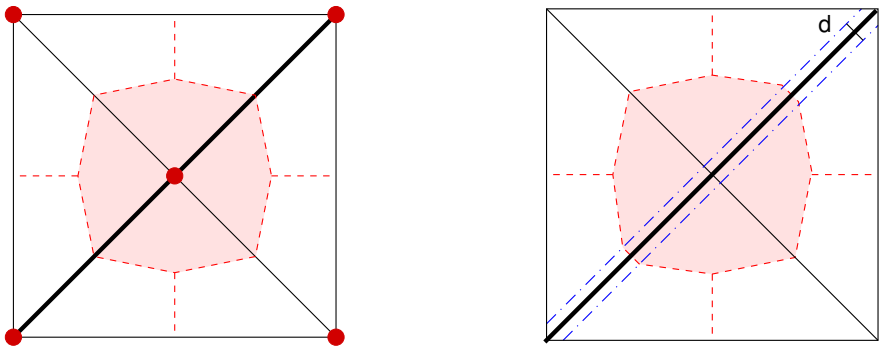

(a) Lower-dimensional 1D fracture

(b) Equi-dimensional 2D fracture

FIGURE 2. Expanding a 1D fracture with associated aperture d to a 2D fracture.

Figure 3 shows the five cases that are most likely to occur in a discretized fracture-matrix system. The control volumes are classified as: (type 1) no fractures, (type 2) a single crossing fracture, (type 3) two crossing fractures, (type 4) a single ending fracture and (type 5) an ending fracture and one passing through. The flux recovery for control volumes is presented here in detail for type 2, and is briefly discussed for the other types afterwards. The expansion procedure for the general case is discussed in Hægland [10].

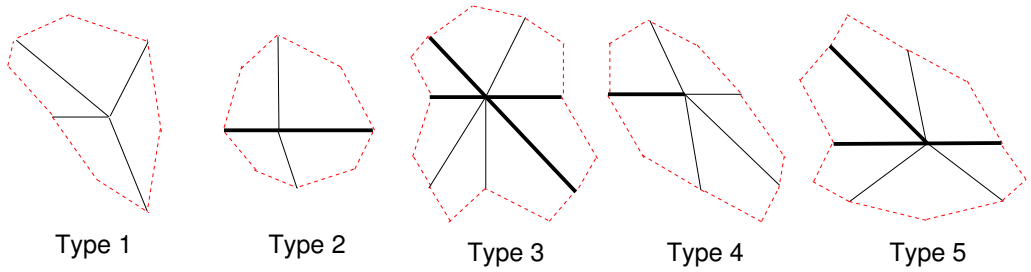

FIGURE 3. The different types of control volumes in a discretized fracture-matrix system. Fractures are indicated with heavy lines.

A simple prototype control volume of type 2 is shown in Figure 4(a). The control volume Ω_{cv} of the central vertex V_5, indicated with the dashed line, is the union of parts of four triangular elements together with a segment of a single fracture, indicated by the heavy line. The control volume comprises a total of N quadrilateral sub control-volumes denoted Q_j, where $j = 1, \ldots, N$ (in this simple case $N = 4$). We order Q_j counter clockwise such that the common edge between Q_1 and Q_N coincides with the fracture. The 1D fracture is expanded to a 2D fracture with aperture d, such that two new rectangular sub control-volumes Q_1^f and Q_2^f are created inside the control volume, see Figure 4(b). Each quadrilateral Q_j is split into two triangles, one interior T_j^{int} and one exterior T_j^{ext}, relative to the central node of the control volume, see Figure 4(b). The lines separating the triangles T_j^{int} and T_j^{ext} are denoted E_j^{ext}. Only the part of the control volume composed of the interior triangles T_j^{int} and the fracture sub control-volumes Q_1^f and Q_2^f is considered in the flux recovery, see Figure 4(c).

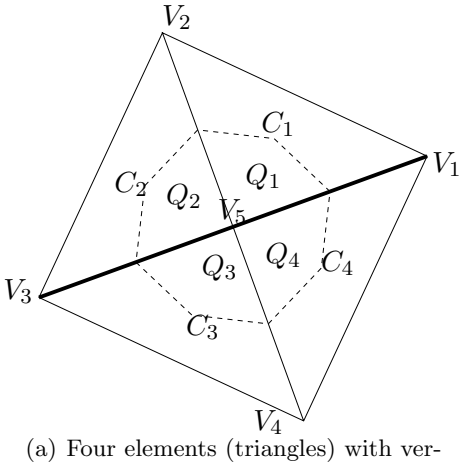

(a) Four elements (triangles) with vertices $V_1, \ldots, V_5$. A control volume (dashed line) is associated with V_5.

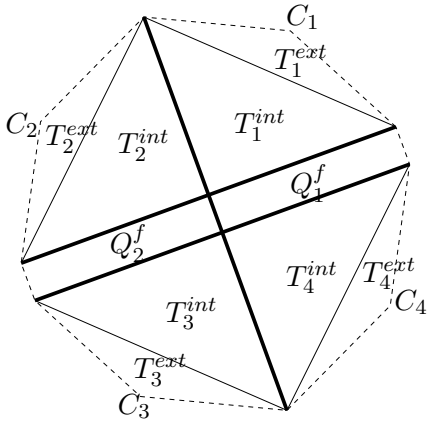

(b) The control volume in the left figure. The fracture has been expanded to a 2D element with aperture d.

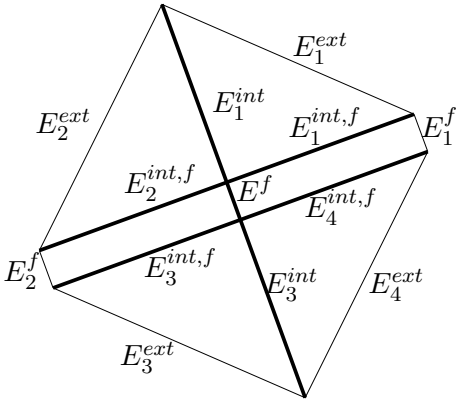

(c) Control-volume edge numbering

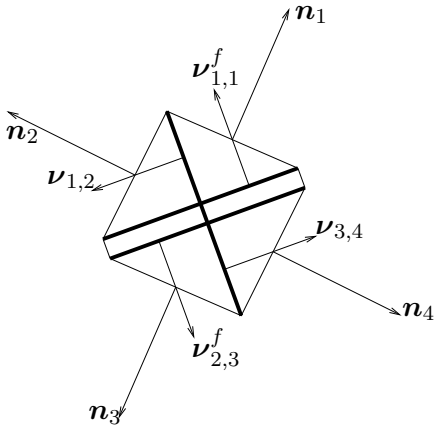

(d) Control-volume normal vectors

FIGURE 4. Flux recovery for a control volume with an internal fracture.

From the flow simulation, fluxes are given over the exterior faces of the control volume Ω_{cv}, as indicated by the dashed line segments in Figure 4(b). The recovery procedure calculates additional conservative fluxes on the interior matrix edges (E_j^{int} and $E_j^{int,f}$) and the interior fracture edge (E^f), see Figure 4(c). These fluxes on E_j^{int} and $E_j^{int,f}$ are obtained indirectly by computing a constant Darcy velocity $\boldsymbol{q}_j$ of each interior triangle T_j^{int}.

The constant Darcy velocities $\boldsymbol{q}_j$ and the fracture interior fluxes F^f must satisfy the following conditions

- mass conservation for the exterior triangle T_j^{ext}:

$$\boldsymbol{q}_j \cdot \boldsymbol{n}_j \;=\; F_{j,1} + F_{j,2}\;, \qquad j = 1, \ldots, N\;, \tag{3}$$

where $\boldsymbol{n}_j$ is the outward normal vector to E_j^{ext} relative to T_j^{ext} with its length equal to the length of the edge E_j^{ext}, see Figure 4(d). Fluxes $F_{j,1}$ and $F_{j,2}$ are the given fluxes with respect to the outward normal vector of T_j^{ext} at the two edges of T_j^{ext} which coincides with the $\partial\Omega_{cv}$, see Figure 4(b).

- the flux over the interior boundaries not coinciding with the fracture edges must be continuous:

$$\boldsymbol{q}_j \cdot \boldsymbol{\nu}_{j,j+1} \;=\; \boldsymbol{q}_{j+1} \cdot \boldsymbol{\nu}_{j,j+1} \;, \qquad j = 1, \ldots, M-1, M+1, \ldots, N-1 \;, \tag{4}$$

  where M is the number of the last interior triangle belonging to Ω_1, $\boldsymbol{\nu}_{j,j+1}$ is the normal vector of the interior boundary E_j^{int} pointing from T_j^{int} to T_{j+1}^{int} and has length equal to E_j^{int}, see Figure 4(d).
- mass conservation in one fracture Q_k^f is required:

$$-\boldsymbol{q}_j \cdot \boldsymbol{\nu}_{k,j}^f + \boldsymbol{q}_{j+1} \cdot \boldsymbol{\nu}_{k,j}^f + F^f + F_k^f \;=\; 0 \;, \tag{5}$$

  where F^f is the unknown flux over the fracture interior edge E^f, F_k^f is the given flux over the edge of the expanded fracture Q_k^f, which coincides with a part of the boundary of the expanded control volume. The sign of the fluxes are chosen according to the outward normal vector of Q_k^f. Further, $\boldsymbol{\nu}_{k,j}^f$ is a normal vector to the edge $E_j^{int,f}$ between the fracture k and the interior triangle T_j^{int} and has its length equal to the edge. The sign of $\boldsymbol{\nu}_{k,j}^f$ is chosen as shown in Figure 4(d). Note that we consider only one mass conservation for one of the fracture quadrilaterals; mass conservation for the other is automatically fulfilled since the sum of the fluxes out of Ω_{cv} is zero.

A system of $2N-1$ linear equations has now been set up, however, a total number of unknown components $2N+1$ ($2N$ from the $\boldsymbol{q}_j$ and 1 from the flux F^f) must be determined. To close the system, we need two more equations, which can be derived by requiring the gradient of the pressure field to be irrotational ([6]). From Equation (2), the Darcy velocity $\boldsymbol{q}$ can be written as

$$\boldsymbol{q} = -\frac{\boldsymbol{K}}{\mu} \nabla p \;. \tag{6}$$

Rearranging Equation (6) and taking the curl of a gradient yield

$$\nabla \times \mu \boldsymbol{K}^{-1} \boldsymbol{q} = -\nabla \times \nabla p \;. \tag{7}$$

Since the curl of a gradient is always zero and the dynamic viscosity μ is constant in this study, we have from Stokes theorem

$$\int_\Omega \nabla \times \boldsymbol{K}^{-1} \boldsymbol{q} d\Omega = \oint_\Gamma \boldsymbol{K}^{-1} \boldsymbol{q} \cdot d\boldsymbol{s} = 0 \;. \tag{8}$$

Here, Ω may be any 2D subdomain of the whole solution domain, and Γ is the 1D boundary of Ω. Equation (8) is now applied over two subdomains, Ω_1 and Ω_2, separated by the fracture.

For this simple case shown in Figure 4(c), the subdomain Ω_1 contains T_1^{int} and T_2^{int} with its boundary Γ_1 corresponding to the counter clockwise sequences of edges E_1^{ext}, E_2^{ext}, $E_2^{int,f}$ and $E_1^{int,f}$. Then, Equation (8) can be written as

$$\oint_{\Gamma_1} \boldsymbol{K}^{-1} \boldsymbol{q} \cdot d\boldsymbol{s} \;=\; \sum_{j=1}^{M} \int_{E_j^{ext}} \boldsymbol{K}_j^{-1} \boldsymbol{q}_j \cdot d\boldsymbol{s} + \int_{E_2^{int,f}} K_F^{-1} \boldsymbol{q}_2^f \cdot d\boldsymbol{s} + \int_{E_1^{int,f}} K_F^{-1} \boldsymbol{q}_1^f \cdot d\boldsymbol{s} \;= 0 \;, \tag{9}$$

where the orientation of integration is counter clockwise, M is the number of the last interior triangle belonging to Ω_1 (here $M = 2$), and the fracture permeability K_F is a scalar.

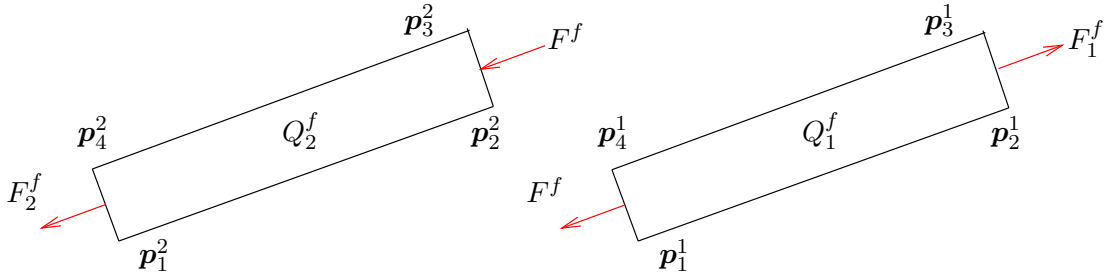

FIGURE 5. The four corners points and the direction of fluxes of the fracture rectangles.

In the first term of Equation (9), both $\boldsymbol{K}_j$ and $\boldsymbol{q}_j$ are constant; hence,

$$\sum_{j=1}^{M} \int_{E_j^{ext}} \boldsymbol{K}_j^{-1}\boldsymbol{q}_j \cdot d\boldsymbol{s} = \sum_{j=1}^{M} \boldsymbol{K}_j^{-1}\boldsymbol{q}_j \cdot \boldsymbol{t}_j = \sum_{j=1}^{M} \boldsymbol{K}_j^{-1}\boldsymbol{t}_j \cdot \boldsymbol{q}_j \ , \tag{10}$$

where the tangent vectors $\boldsymbol{t}_j$ corresponds to a 90 degrees counter-clockwise rotation of the normal vector $\boldsymbol{n}_j$ having the length of E_j^{ext}.
The second and the third terms in Equation (9) are integrals along the fracture edges. The velocities in the fracture quadrilaterals $\boldsymbol{q}_1^f$ and $\boldsymbol{q}_2^f$ are given by linear interpolation of the edge fluxes using Pollock's method [20]. This yields

$$\int_{E_2^{int,f}} K_F^{-1}\boldsymbol{q}_2^f \cdot d\boldsymbol{s} = \frac{(-F_2^f - F^f)\|\boldsymbol{u}_2\|}{2K_F\|\boldsymbol{v}_2\|} \ , \tag{11}$$

and

$$\int_{E_1^{int,f}} K_F^{-1}\boldsymbol{q}_1^f \cdot d\boldsymbol{s} = \frac{(F_1^f - F^f)\|\boldsymbol{u}_1\|}{2K_F\|\boldsymbol{v}_1\|} \ , \tag{12}$$

where

$$\boldsymbol{u}_k = \boldsymbol{p}_2^k - \boldsymbol{p}_1^k \qquad \text{and} \qquad \boldsymbol{v}_k = \boldsymbol{p}_4^k - \boldsymbol{p}_1^k \ , \qquad k = 1, 2 \ . \tag{13}$$

As shown in Figure 5, $\boldsymbol{p}_i^k$ is the coordinate of the corners i of an extended fracture Q_k^f and F_i^f is the flux over the fracture exterior edge E_k^f given from the flow simulation. The details of the calculation leading to Equations (11) and (12) are presented in the Appendix.

Substituting Equations (10) - (12) in Equation (9) yields

$$\oint_{\Gamma_1} \boldsymbol{K}^{-1}\boldsymbol{q} \cdot d\boldsymbol{s} = \sum_{j=1}^{M} \boldsymbol{K}_j^{-1}\boldsymbol{t}_j \cdot \boldsymbol{q}_j + \frac{(-F_2^f - F^f)\|\boldsymbol{u}_2\|}{2K_F\|\boldsymbol{v}_2\|} + \frac{(F_1^f - F^f)\|\boldsymbol{u}_1\|}{2K_F\|\boldsymbol{v}_1\|} \ . \tag{14}$$

A similar argument can be used to show that the line integral along Γ_2 can be given as

$$\oint_{\Gamma_2} \boldsymbol{K}^{-1}\boldsymbol{q} \cdot d\boldsymbol{s} = \sum_{j=M+1}^{N} \boldsymbol{K}_j^{-1}\boldsymbol{t}_j \cdot \boldsymbol{q}_j - \frac{(F_1^f - F^f)\|\boldsymbol{u}_1\|}{2K_F\|\boldsymbol{v}_1\|} - \frac{(-F_2^f - F^f)\|\boldsymbol{u}_2\|}{2K_F\|\boldsymbol{v}_2\|} \ . \tag{15}$$

The general case of a discretized fracture-matrix control volume is described by ϱ fractures meeting at a vertex ($\varrho = 0, 1, 2, ...$). A new mesh of expanded fractures is constructed by introducing a polygon $\mathcal{M}$ with ϱ edges at the overlapping area of the ϱ expanded fractures. The ϱ fractures now becomes ϱ trapezoidal elements and the central polygon $\mathcal{M}$ is divided into ϱ triangles, each having one vertex at the centroid of the polygon. A sketch of a case for $\varrho = 5$ is shown in Figure 6. The flux recovery method for two fractures described

previously can now be extended to the case of ϱ fractures. The exterior flux continuity shown in Equation (3) remains the same. However, the interior continuity equations shown in Equation (4) is reduced from $N-2$ to $N-\varrho$ due to the presence of more fractures within the control volume. Furthermore, there are now ϱ fractures for which Equation (5) has to be imposed. These increased constraints are counterbalanced by an increased number of unknown fracture fluxes F_k^f in Equation (5). Next, Equations (14) and (15) have to be extended to ϱ curl relations, instead of two. Finally, after the system of equations are solved, the solution of the fracture fluxes F_k^f are then used to compute the interior fluxes of the triangles of the central polygon $\mathcal{M}$ by following the original method of Cordes and Kinzelbach [6].

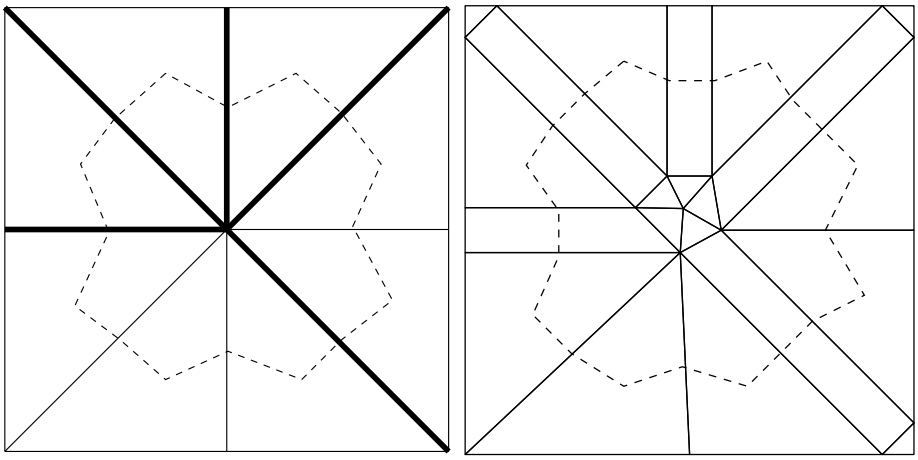

FIGURE 6. Five fracture meeting. Left: Unexpanded fractures. Right: Expanded fractures.

For other types of control volumes, a similar concept of the fracture extension and the flux recovery are applied. The system of equations are solved based on Equations (3), (4), (5), (14) and (15).

This work do not consider the 3D case, however extension of the flux recovery procedure to the 3D case without fractures has been considered by Prévost [21]. A difficulty with the 3D case compared to the 2D case is that in 3D there are more faces connected to a vertex than there are elements. In 2D, the number of edges and the number of elements connected to a vertex were the same, which allowed a straight forward derivation of the linear system. In 3D, additional constraints must be devised to close the system, or the system can be solved in least-square sense, see [21]. The expansion of the fractures for the 3D case is discussed in Hægland [10].

2.3. **Streamline tracing.** A streamline $\boldsymbol{s}(\tau)$ is defined by requiring that the tangent of the streamline should be equal to the velocity,

$$\frac{d\boldsymbol{s}}{d\tau} = \frac{\boldsymbol{q}(\boldsymbol{x})}{\phi} \,, \tag{16}$$

where τ is the streamline parameter denoted the time-of-flight (TOF), $\boldsymbol{q}$ is the Darcy velocity, and ϕ is the porosity. By rearranging Equation (16) and integrating with respect to the arc length of a streamline, the TOF that a particle need to travel a given distance s is given by,

$$\tau(s) = \int_0^s \frac{\phi}{\|\boldsymbol{q}\|} ds', \tag{17}$$

where s measures arc length along a streamline. Note that, due to the appearance of the porosity in Equation (17), the TOF is related to the particle velocity, not the Darcy velocity.

Methods for streamline tracing on quadrilateral grids when fluxes are known have been investigated by several authors. For a regular quadrilateral mesh (rectangular mesh) Pollock's method has been widely used. The method assumes a piece-wise linear approximation of the velocity over the entire grid. Within a single grid cell taken to be the unit square for simplicity, the velocity is given as

$$\boldsymbol{q}(\boldsymbol{x}) = \begin{bmatrix} f_{x0}(1-x) + f_{x1}x \\ f_{y0}(1-y) + f_{y1}y \end{bmatrix}, \qquad 0 \le x \le 1 \quad \text{and} \quad 0 \le y \le 1\,, \tag{18}$$

where f_k are fluxes over the cell faces (see Figure 7). Solving Equation (16) by inserting the velocity from Equation (18) yields two separate expressions for the TOF:

$$\tau_x(x_i, x_j) = \frac{\phi}{f_{x1} - f_{x0}} \ln\left(\frac{f_{x0} + (f_{x1} - f_{x0})x_j}{f_{x0} + (f_{x1} - f_{x0})x_i}\right), \tag{19}$$

and

$$\tau_y(y_i, y_j) = \frac{\phi}{f_{y1} - f_{y0}} \ln\left(\frac{f_{y0} + (f_{y1} - f_{y0})y_j}{f_{y0} + (f_{y1} - f_{y0})y_i}\right). \tag{20}$$

The TOF that a particle travels from the entry point $\boldsymbol{x}_{en}$ to the exit point $\boldsymbol{x}_{ex}$ of the grid cell is determined by calculating the time that a streamline requires to cross the grid boundaries. Inserting $x_j = 0$ and 1 in Equation (19) and $y_j = 0$ and 1 in Equation (20), and replacing x_i and y_i with $\boldsymbol{x}_{en}$ yield four different times that the streamline requires to cross the left, the right, the bottom and the top boundaries respectively. The TOF is the minimum positive time of the calculated times. By rearranging Equations (19) and (20) and inserting the TOF in τ_{ex}, the exit point $\boldsymbol{x}_{ex}$ is then given as

$$x_{ex} = \frac{1}{f_{x1} - f_{x0}} \left\{ q_{en,x} \exp\left(\frac{\tau_{ex}}{\phi}(f_{x1} - f_{x0})\right) - f_{x0} \right\}, \tag{21}$$

$$y_{ex} = \frac{1}{f_{y1} - f_{y0}} \left\{ q_{en,y} \exp\left(\frac{\tau_{ex}}{\phi}(f_{y1} - f_{y0})\right) - f_{y0} \right\}, \tag{22}$$

where $\boldsymbol{q}_{en}$ is the velocity at the entry point $\boldsymbol{x}_{en}$ calculated from Equation (18).

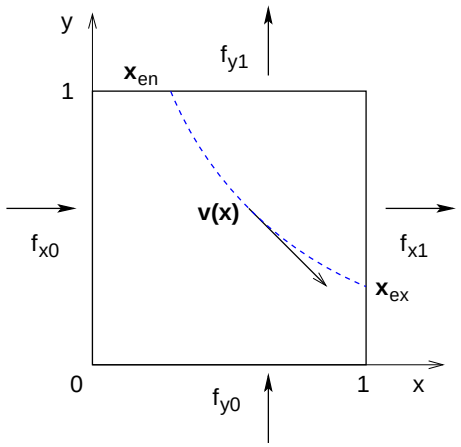

FIGURE 7. Pollock tracing for a unit square.

A complex fracture-matrix system can only be discretized precisely with unstructured grids. Hence, streamline tracing which performs well on unstructured grids is required. The extension of Pollock's method on unstructured grids has proven successful in several studies [6, 22, 11]. The spatial coordinates together with the velocity in the physical space $\mathcal{P}$ are transformed to a reference space $\mathcal{R}$ by using the bilinear iso-parametric transformation, see Figure 8.

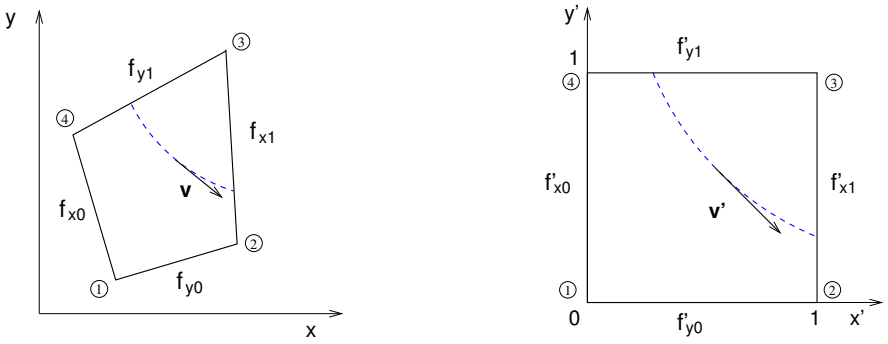

(a) Physical space $\mathcal{P}$ (b) Reference space $\mathcal{R}$

FIGURE 8. Transformation of an unstructured grid and edge fluxes from a physical space $\mathcal{P}$ to a reference space $\mathcal{R}$.

According to Hægland et al. [11], the velocity field $\boldsymbol{v}'$ in $\mathcal{R}$ is related to the linear flux interpolation as

$$\boldsymbol{q}' = \frac{d\boldsymbol{x}'}{dt} = \frac{1}{\det \boldsymbol{J}} \begin{bmatrix} f_{x0}(1-x'_i) + f_{x1}x'_i \\ f_{y0}(1-y'_i) + f_{y1}y'_i \end{bmatrix} , \tag{23}$$

where $\boldsymbol{J}$ is the Jacobian transformation matrix

$$\boldsymbol{J} = \begin{bmatrix} \dfrac{dx}{dx'} & \dfrac{dx}{dy'} \\ \dfrac{dy}{dx'} & \dfrac{dy}{dy'} \end{bmatrix} . \tag{24}$$

The velocity in Equation (23) is rewritten in terms of a pseudo time τ in $\mathcal{R}$ as shown by Jimenez et al. [13] as

$$d\tau = \frac{dt}{\det \boldsymbol{J}} = \begin{bmatrix} \dfrac{dx'}{f_{x0}(1-x'_i) + f_{x1}x'_i} \\ \dfrac{dy'}{f_{y0}(1-y'_i) + f_{y1}y'_i} \end{bmatrix} , \tag{25}$$

where t is real time in $\mathcal{P}$. The actual time-of-flight t_{ex} is then evaluated by integrating Equation (25) from $\boldsymbol{x}'_{en}$ to $\boldsymbol{x}'_{ex}$:

$$t_{ex} = \int_0^{t(\tau_{ex})} dt = \int_0^{\tau_{ex}} \det \boldsymbol{J}(x'(\tau), y'(\tau)) d\tau . \tag{26}$$

Recently, some problems with the method have been reported and resolved. Inaccuracies in computing TOF due to errors in the absolute value of the interpolated velocity field have been reported in [13, 9, 11]. Jimenez et al. [13] proposed an extension of the method that allowed for exact reproduction of time-of-flight for uniform flow in 2D. In this paper, we utilize this latter approach, see [9, 11, 13] for more details of the method.

2.4. **Evaluation of the breakthrough curve.** We assume purely advective transport of a solute tracer in the streamline method and visualize each streamline as a flow channel or a streamtube. Due to the pure advective transport in the streamline method, no mass exchanges between neighboring streamtubes. The TOF measures the time that the tracer needs to travel along the streamtube, see Figure 9. Streamlines are distributed equally according to the total flux along the inflow boundary, such that each streamtube contains the same flux.

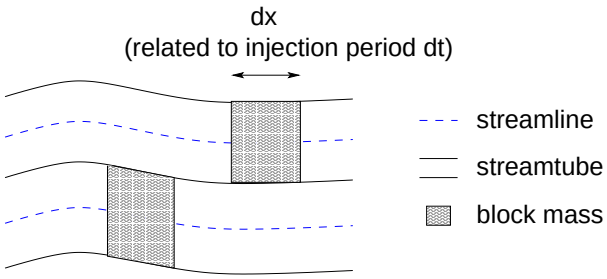

FIGURE 9. Mass transport in a streamtube as a block.

The transport behavior characterized from the results of the streamline method are described using a breakthrough curve (BTC) and an accumulated breakthrough curve (AccBTC). The latter is the sum of the total mass leaving the domain at the outflow boundary until a time t and BTC is the rate of change of AccBTC during the time interval Δt

$$\mathrm{BTC}(t) = \frac{\mathrm{AccBTC}(t) - \mathrm{AccBTC}(t-\Delta t)}{\Delta t}\,, \tag{27}$$

$$\mathrm{AccBTC}(t) = \mathrm{AccBTC}(t-\Delta t) + \dot{m}^s \sum_{i=1}^{n} \mathcal{T}_i\,, \tag{28}$$

where $\dot{m}^s$ is the normalized mass flux, which is determined by the mass flux in each streamtube over the total injected mass, and n is the total number of the streamtubes. The arrival time condition $\mathcal{T}_i$, for a streamtube i, is given as

$$\mathcal{T}_i(t) = \begin{cases} 0 & ; \quad t < \mathrm{TOF}_i \\ t - \mathrm{TOF}_i & ; \quad \mathrm{TOF}_i \le t \le \mathrm{TOF}_i + dt \\ 0 & ; \quad t > \mathrm{TOF}_i + dt \end{cases} \tag{29}$$

where the time of flight TOF_i is the time that a block mass in a streamtube i travels until it reaches the outflow boundary and dt is the duration of mass injection.
The TOF of each streamtube is a discrete value, which can be the same for all streamtubes or highly varied depending on the geometries and structures of a domain. The overall transport behavior of the system is presented as a histogram BTC which evaluates the rate of change of the normalized mass flux over a specified interval of time.

3. Comparison Results

3.1. **Preliminary test case.** In order to understand the difference arising from simulating the transport process using grid-based advective transport (ADT) and the streamline method (STR), three preliminary test cases are set up: a single short fracture, a single long fracture and systematically distributed fractures, see Figure 10 (top). For all test cases, a two-dimensional domain of 1.0×1.0 m is set up. The fluid properties and the domain properties correspond to the data presented in Table 1.

We consider transport of a solute tracer without dispersion and the governing equation can be written as

$$\frac{\partial c}{\partial t} + \nabla \cdot \frac{\boldsymbol{q}}{\phi} c = 0 \,. \tag{30}$$

where c is the concentration of the tracer. For the ADT, Equation (30) is discretized using a box method with upwinding formulation ([19]). For the STR, the transport of solute tracer is obtained directly from the streamline time-of-flight and Equation (28).
The boundary conditions are no-flow on the top and the bottom. For the flow simulation, a Dirichlet boundary in terms of pressure is given on the left-hand side (the inflow boundary) and on the right-hand side (the outflow boundary). For the grid-based transport simulation (ADT), tracer is given for a very short time at the inflow boundary. A free-flow boundary is given at the outflow for the transport simulation, which means that a tracer arriving at the boundary is allowed to leave freely. A total of 500 streamlines are traced and distributed equally according to the fluxes at the inflow. We used 500 streamlines because the AccBTC from 500 streamlines showed visual convergence to the AccBTC from 10000 streamlines.
The ADT and the STR are carried out on different mesh sizes (measured in terms of the average length of the sides of a grid cell) of approximately 0.01, 0.02 and 0.03 m to investigate the influence of numerical diffusion.

		Domain Properties	
		matrix	**fracture**
Permeability, K	$[m^2]$	$1.0 \cdot 10^{-13}$	$8.33 \cdot 10^{-10}$
Eff. porosity, ϕ	[-]	0.13	0.30
Aperture, b	$[m]$	-	$1.0 \cdot 10^{-4}$
		Fluid Properties	
Viscosity, μ	$[kg/(m \cdot s)]$	$1.814 \cdot 10^{-5}$	
Density, ρ	$[kg/m^3]$	1.21	

TABLE 1. Domain and fluid properties for all simulations.

Some streamlines of the fine mesh (0.01 m) are shown in Figure 10 (bottom). In all cases we observed that high permeability in fractures resulted in flow paths towards the fractures. These flow paths yield a faster tracer transport within their streamtubes, whereas the other flow paths in the surrounding matrix lead to a slower tracer transport.
The results of the accumulated breakthrough curves (AccBTCs) and the breakthrough curves (BTCs) are presented in Figure 11. In all test cases, the AccBTCs and the BTCs of the ADT differ considerably between different mesh sizes due to numerical diffusion. Whereas, the AccBTCs from the STR are rather similar for all mesh sizes and their slight local differences come from the fact that the velocity field obtained from the flow simulation is locally grid dependent, especially near the fractures.
In the short fracture case, the BTCs of the ADT in Figures 11a1 show that using a coarser mesh size results in a higher variance and a lower peak value. This indicates that the numerical diffusion increases the spreading of the tracer plume in the matrix and smears out the concentration front, especially the double-continuum effect due to fast transport in the fracture and slow transport in the matrix has disappeared. On the contrary, for the STR having no numerical diffusion, the double-continuum effect results in the two jumps of the AccBTCs (Figure 11a2) and the two peaks of the BTCs (Figure 11a3). The large

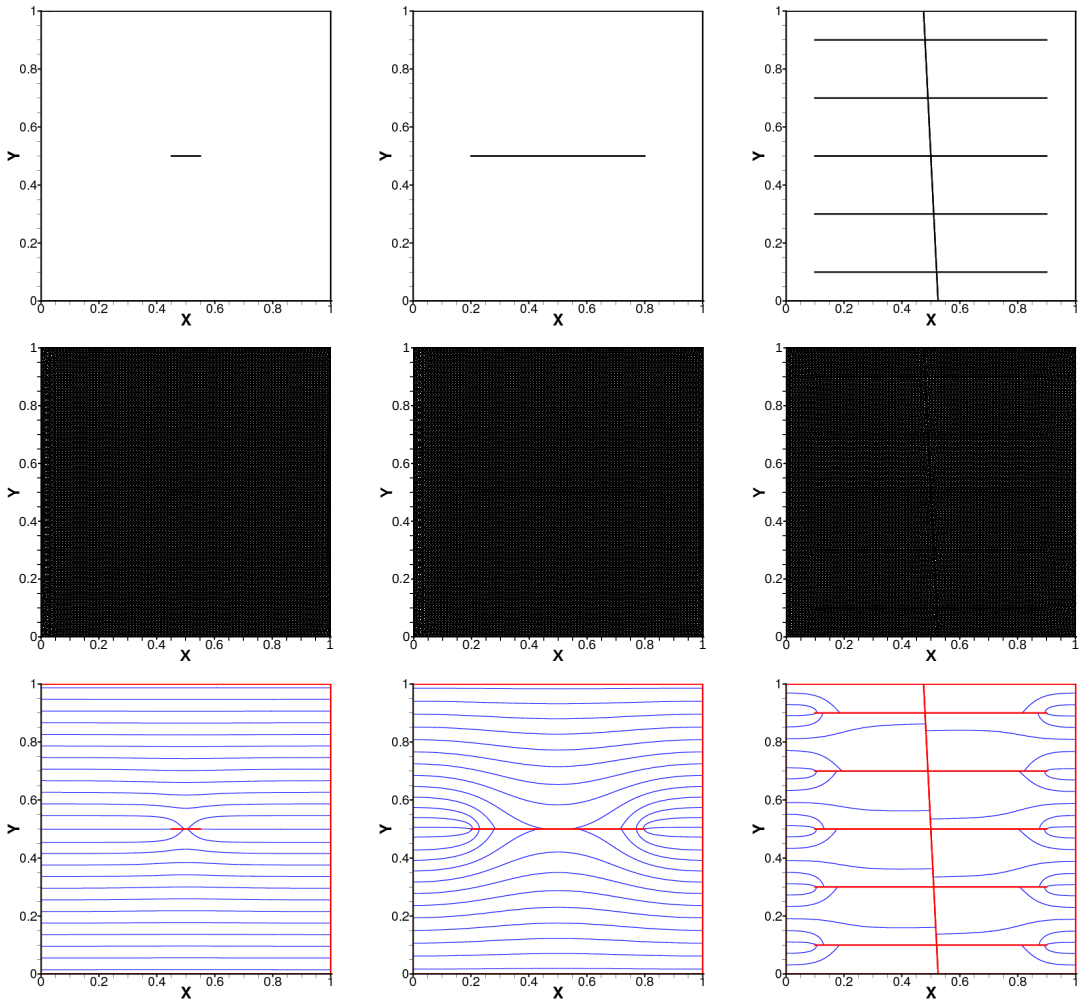

FIGURE 10. Top: Domains with fractures. Middle: Discretization domains (top) for a mesh size of 0.01 m corresponding to ca. 11700 vertices. Bottom: 25 of the 500 streamlines traced for the grids in the middle row.

part of the tracer transported in the matrix arrives about the same time at the outflow and results in a very high mass flux in the second peak of the BTC and a sharp rise of the second jump in the AccBTC.

When the fracture becomes longer (Figure 11b), the double-continuum effect can also be noticed for the ADT, in spite of the numerical diffusion, see Figures 11b1 and 11b2. The fast transport in the long fracture results in the first peak of the BTCs; later, the part of the tracer plume transported in the matrix leads to the second peak. The numerical diffusion in the transversal flow-direction causes spreading of mass transported in the fracture to the surrounding matrix. Therefore, the value of the first peak of the BTC of the STR is higher than that of the ADT (see Figure 11b3) and the AccBTCs show a sharp rise for the STR, but only a gradual increase for the ADT (see Figures 11b2). This effect delays the arrival time of the mass transported in the fracture. The influence of the numerical diffusion on the part of the tracer transported through the porous matrix shows the same behavior as that observed in the BTCs for the single short fracture, as discussed above.

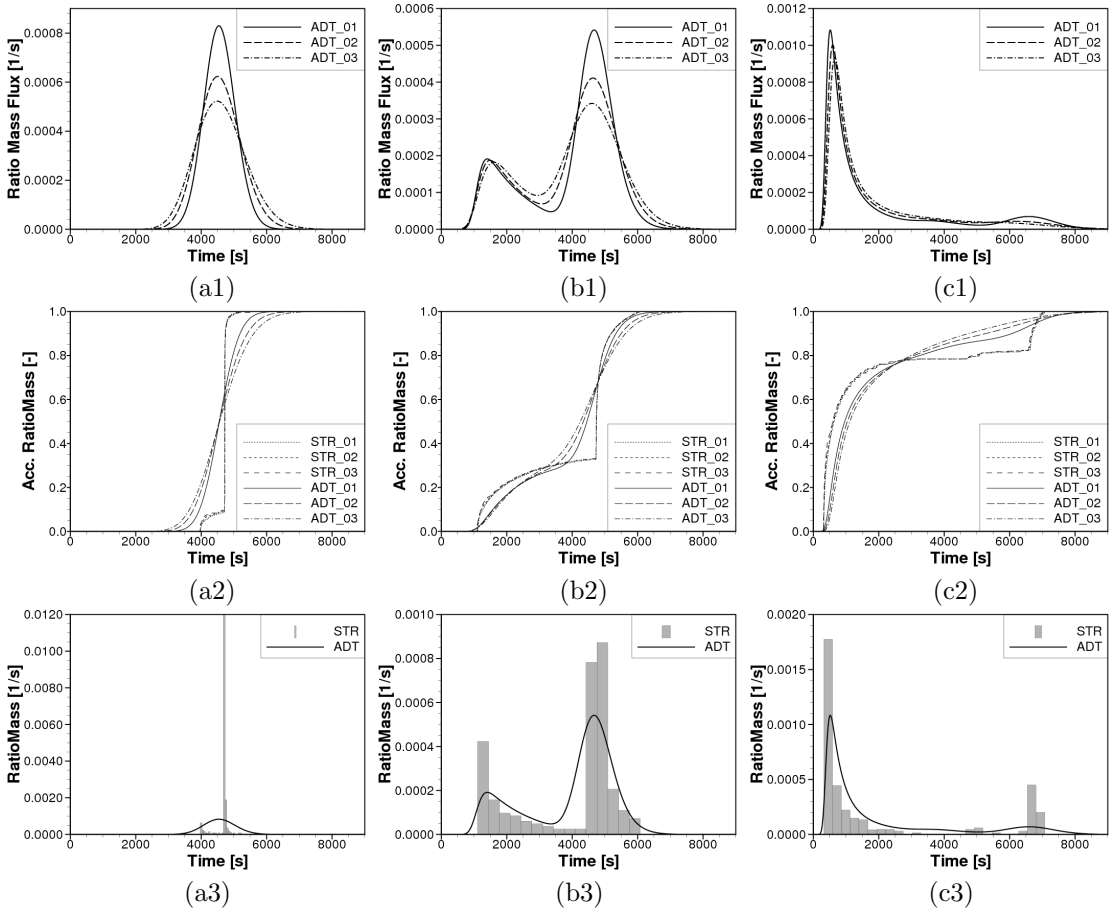

FIGURE 11. Transport simulation results of ADT and STR for the test cases: a) (left column) a single short fracture, b) (middle column) a single long fracture and c) (right column) systematically distributed fractures. Top row (a1/b1/c1): BTC of ADT for different mesh sizes. Middle row (a2/b2/c2): AccBTC of ADT and STR for different mesh sizes. Bottom row (a3/b3/c3): BTC of ADT and STR at a mesh size of 0.01 m.

Increasing the number of horizontal fractures with a vertical fracture connecting all horizontal fractures (Figure 11c) increases the part of tracer transported in the fractures and decreases the part transported in the matrix. Therefore, the BTCs in Figure 11c1 show a high peak and the AccBTCs in Figure 11c2 show a high first jump. Due to the influence of the numerical diffusion in the ADT, the BTCs of the coarse mesh size of 0.03 and 0.02 m show only a long tail, whereas the BTC of the fine mesh size of 0.01 m has a small second peak (see Figure 11c1), more similar to the BTC of the STR showing a double-continuum effect as can be seen in Figure 11c3. The effect of the numerical diffusion along fractures in the transversal flow-direction can be better noticed in this case than in the single long fracture case. As the mesh gets finer and the numerical diffusion decreases, the tracer transported in the fractures remains more confined to the fractures and arrives faster at the outflow and this yields a BTC with a slightly higher peak concentration shifted somewhat to the left compared to the BTCs of the coarser mesh sizes (see Figure 11c1). The AccBTCs of the ADT seem to converge to the result of the STR when the mesh becomes finer and the numerical diffusion decreases, see Figure 11c2.

3.2. **A complex fracture-matrix system.** After a basic understanding of the transport behavior for ADT and STR has been gained from the preliminary test cases, the next step is to perform a comparison study between the two approaches in a complex fracture-matrix system. The fracture networks are generated by the fracture generator FRAC3D based on statistical geometries and geostatistical parameters taken from a study site in Pliezhausen, Germany, see [2, 3]. Boundary conditions, fluid properties, and domain properties are the same as for the test cases in the previous section.
We consider five different cases (GFG-A, GFG-B, GFG-C, SFG-A and SFG-B) where their fracture networks are generated from five different geometries and spatial characteristics using a statistical or geostatistical approach as described in the associated paper ([3]). Several realizations of a fracture network with the same fracture geometries and spatial characteristics can be obtained when a fracture network is generated based on a stochastical approach. In this study, for each of the five cases we consider five fracture-network realizations. We first consider the five realizations from the GFG-A, and subsequently consider the average behavior of the five realizations from each of the cases.
We start by generating five realizations R1-R5 from the GFG-A. The streamline distribution taken from realization R1 is shown in Figure 12. In a complex fracture-matrix system, the increased number of fractures and varying orientations lead to a high dispersion of the tracer plume. As shown in Figure 12, no streamlines are transported only in the surrounding matrix, but rather they are partly transported in the fractures and partly in the matrix. Hence, the AccBTCs of the five realizations do not show a clear double-continuum behavior, see Figure 13. For all realizations, the AccBTCs of the STR shift to the left compared with the ADT which means that in the STR simulation mass transports faster than in the ADT simulation. This corresponds with the results presented in the case of systematically distributed fractures. The numerical diffusion in the ADT leads to a delay of mass transport in the fractures.

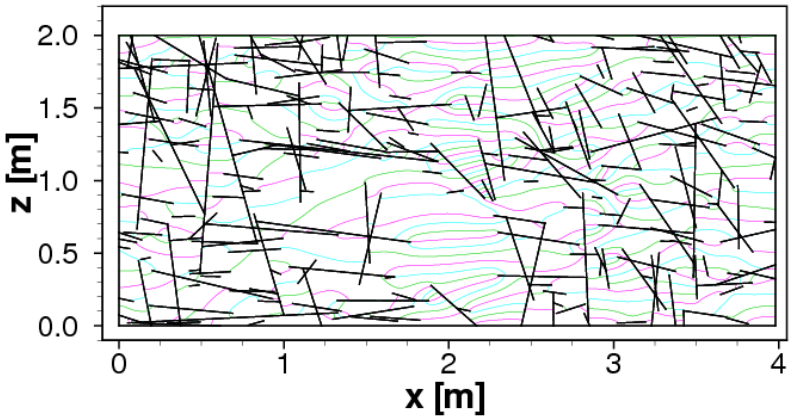

FIGURE 12. Streamlines traced for one realization (R1) of a complex fracture-matrix system of the GFG-A.

The transport behavior is characterized by the effective travel time, the variance and the skewness and they are evaluated from the moment and the central moment of the BTC ([3]). The variance and the skewness of the BTC depend highly on the distribution of the tracer concentration. A high variance means a high degree of spreading of the plume. The skewness represents the asymmetry of the spreading. A positive skewness indicates that a larger part of tracer plume first transports to the outflow, and then the rest of the

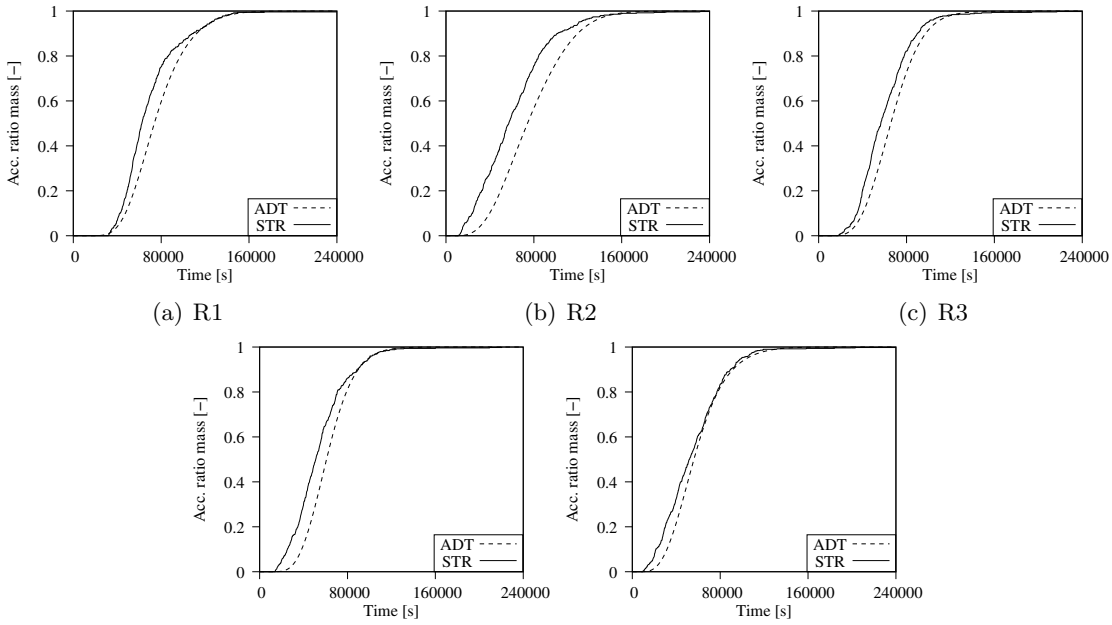

(a) R1 (b) R2 (c) R3

(d) R4 (e) R5

FIGURE 13. AccBTCs of ADT and STR for the complex fracture-matrix systems for five realizations (R1-R5) of the GFG-A.

plume arrives gradually. The faster mass transport in the STR leads to a less effective travel time compared with the transport in the ADT (see Figure 14a). For all realizations, higher variances and higher skewnesses are seen in the STR compared to the ADT (see Figures 14b and 14c). This is due to the fact that the fast transport in the fractures and the slow transport in the matrix are better captured with the STR, whereas the numerical diffusion in the ADT smears out this contrast.

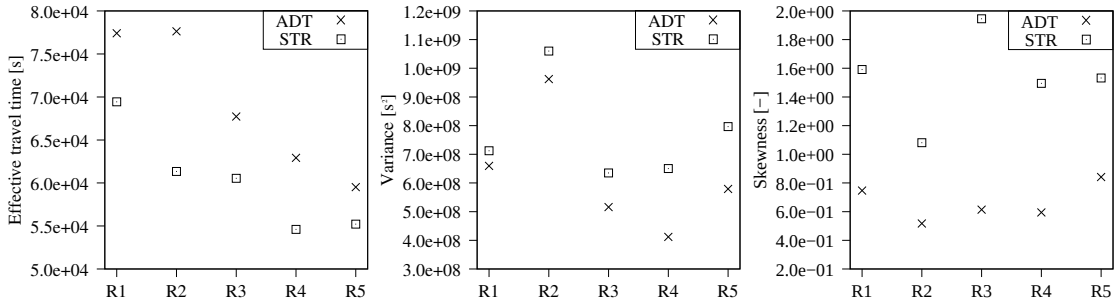

(a) Effective travel time. (b) Variance. (c) Skewness.

FIGURE 14. Quantitative results of ADT and STR for the complex fracture-matrix systems of five realizations from the GFG-A.

In the last part of this section we consider the average behavior for the five cases GFG-A, GFG-B, GFG-C, SFG-A and SFG-B. The details about the fracture generation are presented in the associated paper ([3]). For each case, five realizations are generated and the results presented for each case are the average values over all five realizations.

The average AccBTCs from the STR and the ADT for the five cases are shown in Figure 15. For all five study cases, the average AccBTCs from the STR shifts to the left compared with the ADT which means that the STR leads to a faster mass transport compared to the ADT. This agrees with the average values of the effective travel times of the STR being less than those of the ADT, as shown in Figure 16a. In all cases, a physical dispersion due to fast and slow transport can be identified from the positive skewness in Figure 16c. Due to the purely advective transport and no numerical diffusion in the STR, the variance and the skewness for the STR are larger than for the ADT, indicating a larger physical dispersion. On the other hand, the numerical diffusion in the ADT delays plume migration in the fracture-matrix system. As a result, the difference between AccBTCs and BTCs of the two approaches is clearly noticed for all study cases of the fracture-matrix system. Most of the values obtained from the STR show larger extreme values than from the ADT, particularly for the variance of the SFG-B. Hence, more realizations might be required to represent the transport behavior using STR.

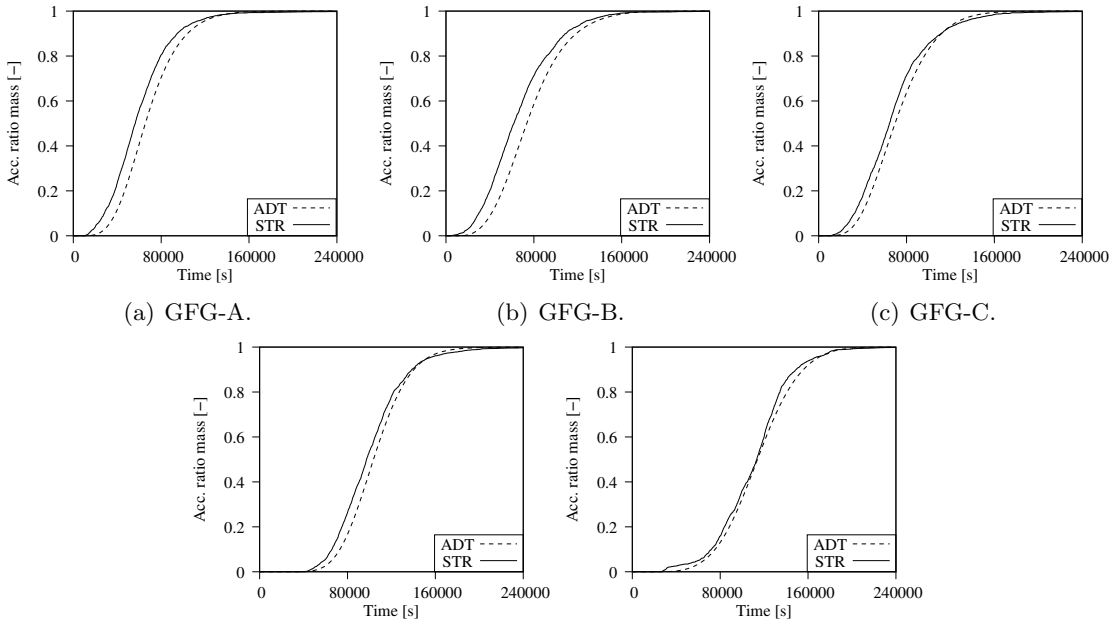

(a) GFG-A. (b) GFG-B. (c) GFG-C.

(d) SFG-A. (e) SFG-B.

FIGURE 15. Average AccBTCs of ADT and STR for the complex fracture-matrix systems for the five different cases GFG-A, GFG-B, GFG-C, SFG-A and SFG-B.

4. Conclusion

The precision of streamline tracing strongly depends on the accuracy of the velocity field. Approximating the fluxes from pressure gradients obtained from the flow simulation results in discontinuous fluxes at element boundaries. A flux recovery for a two-dimensional fracture-matrix system is proposed for calculating mass conservative fluxes over boundaries of quadrilateral sub control-volumes. Lower-dimensional fractures, which are assumed in the flow simulation, have to be extended to equi-dimensional fractures to obtain well defined velocities and streamlines in the fractures (not only parallel to the orientation of the fractures).

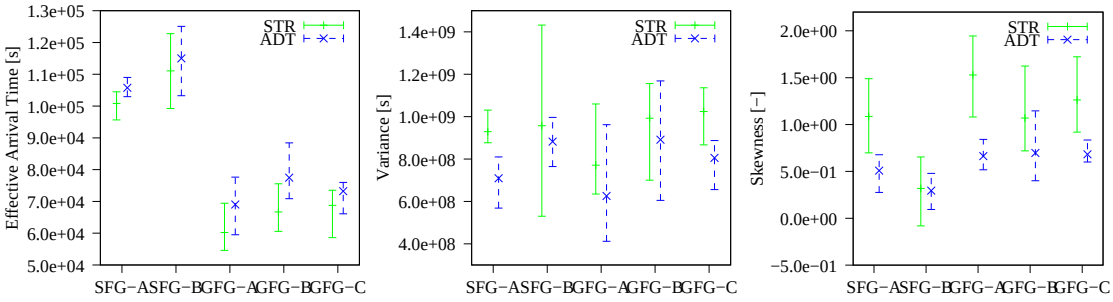

(a) Effective travel time. (b) Variance. (c) Skewness.

FIGURE 16. Average and extreme values (min./max.) obtained from the ADT and the STR for the complex fracture-matrix systems for the five different cases.

The applicability of a streamline method (STR) for the study of the transport behavior in a fracture-matrix system is investigated by comparing with the results from a grid-based advective transport (ADT) model. In the simple cases of one fracture or systematically distributed fractures, the effect of fast flow in the fractures and slow flow in the matrix is smeared out due to the numerical diffusion in the ADT. The preferential flow paths in the fracture-matrix system are clearly noticed in the STR from the double-peak BTCs and two sudden rises in the AccBTCs. In the complex fracture-matrix system consisting of a large number of fractures with varying orientations, numerical diffusion in the ADT delays plume migration, whereas purely advective transport in the STR leads to fast solute transport and maintains a high physical dispersion due to the fast transport in the fractures and slow transport in the matrix. As a result, we observe a less effective travel time, higher variance and higher skewness from the STR than from the ADT as well as a shift of AccBTC of the STR to the left.
Further investigations involving comparisons with experimental or field studies have to be carried out in order to validate the results of the STR. If the assumption of the purely advective transport in the STR leads to an acceleration of the tracer transport in the system compared with the measurement results, including dispersive transport in the STR could be considered to improve the STR approach.

5. APPENDIX

The integral of the velocity along the fracture edge is computed by assuming that the velocities in the quadrilateral fracture are given by linear interpolation of the edge fluxes similar to Pollock's method ([20]). Following Prévost et al. [22] and Jimenez et al. [13], the rectangle Q_1^f (see Figure 4(b)) in $\mathcal{P}$ is transformed to a unit square in a reference space $\mathcal{R}$ using the bilinear transformation $\boldsymbol{x}(\hat{x}, \hat{y})$, which simplifies for a rectangle (Figure 17 (right)) to,

$$\boldsymbol{p}(\hat{x}, \hat{y}) = \boldsymbol{p}_1 + (\boldsymbol{p}_2 - \boldsymbol{p}_1)\hat{x} + (\boldsymbol{p}_4 - \boldsymbol{p}_1)\hat{y} \,, \tag{31}$$

with the constant Jacobian matrix,

$$\boldsymbol{J} = \begin{bmatrix} x_2 - x_1 & x_4 - x_1 \\ y_2 - y_1 & y_4 - y_1 \end{bmatrix} = \begin{bmatrix} \boldsymbol{u} & \boldsymbol{v} \end{bmatrix} , \tag{32}$$

where $\boldsymbol{u}$ and $\boldsymbol{v}$ are the shape vectors of the rectangle, and $\boldsymbol{x}_i$ is the point at corner i see Figure 17 (left). Edge fluxes F_{x0}, F_{x1}, F_{y0}, and F_{y1}, are defined for Q_1^f with positive

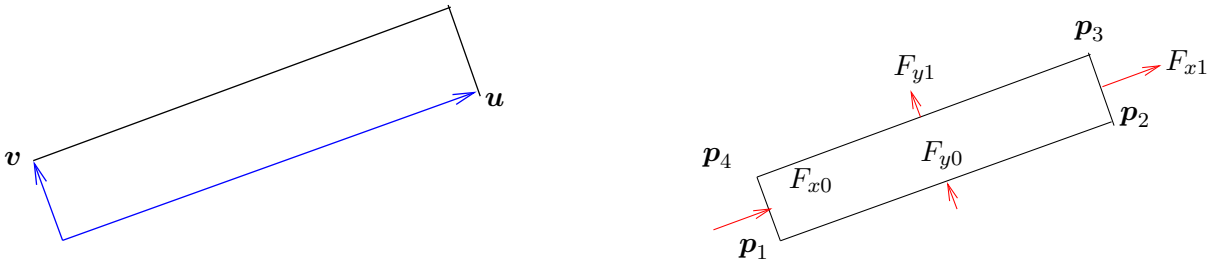

FIGURE 17. The extended fracture rectangle. Left: Shape vectors. Right: Corners and direction of fluxes.

direction as shown in Figure 5 (right). Then, the interpolated velocity $\boldsymbol{q}^f$ in Q_1^f is defined in $\mathcal{R}$ by ([22])

$$\hat{\boldsymbol{q}}^f = \frac{1}{\det \boldsymbol{J}} \begin{bmatrix} F_{x0}(1-\hat{x}) + F_{x1}\hat{x} \\ F_{y0}(1-\hat{x}) + F_{y1}\hat{x} \end{bmatrix}, \tag{33}$$

where the determinant of the Jacobian, $\det \boldsymbol{J}$, is simply equal to the area A of the rectangle. The fluxes F_{y0} and F_{y1} over the edges for the expanded fracture segment Q_1^f are given by the dot product of the constant velocity in the neighboring interior triangle of the fracture and the normal vector of the edge. The sign of the fluxes are indicated in Figure 17 (right). The flux F_{x1} and F_{x0} are given by the unknown interior fracture flux F^f and the flux at fracture flux point respectively. For the expanded fracture segment Q_1^f in Section 2.2, $F_{x0} = -F^f$, $F_{x1} = F_1$, $F_{y0} = -\boldsymbol{q}_N \cdot \boldsymbol{\nu}_{1,1}^f$, and $F_{y1} = -\boldsymbol{q}_1 \cdot \boldsymbol{\nu}_{1,1}^f$. The relation between the velocity in $\mathcal{P}$ and $\mathcal{R}$ is ([11])

$$\boldsymbol{q}^f \;=\; \boldsymbol{J}\hat{\boldsymbol{q}}^f \;=\; \frac{1}{A_1}\left[(F_{x0}(1-\hat{x}) + F_{x1}\hat{x})\boldsymbol{u} + (F_{y0}(1-\hat{y}) + F_{y1}\hat{y})\boldsymbol{v}\right] .$$

The last term in Equation (8) can now be evaluated. We parameterize the path along the fracture edge from $\boldsymbol{p}_4$ to $\boldsymbol{p}_3$ (Figure 17 (right)) as

$$\boldsymbol{\alpha}(\hat{x}) = \boldsymbol{p}(\hat{x}, 1), \qquad 0 \le \hat{x} \le 1 . \tag{34}$$

Then $\boldsymbol{\alpha}'(\hat{x}) = \boldsymbol{u}_1$, and using that $\boldsymbol{u}_1 \cdot \boldsymbol{v}_1 = 0$, $\boldsymbol{u}_1 \cdot \boldsymbol{u}_1 = \|\boldsymbol{u}_1\|^2$, and $A_1 = \|\boldsymbol{u}_1\|\|\boldsymbol{v}_1\|$, we have

$$\begin{aligned} \int_{E_1^{int,f}} K_F^{-1}\boldsymbol{q}_1^f \cdot d\boldsymbol{s} \;&=\; \int_0^1 K_F^{-1}\boldsymbol{q}_1^f(\boldsymbol{\alpha}(\hat{x})) \cdot \boldsymbol{\alpha}'(\hat{x}) d\hat{x} \\ &=\; \frac{1}{A_1}\int_0^1 (F_{x0}(1-\hat{x}) + F_{x1}\hat{x}) K_F^{-1}\boldsymbol{u}_1 \cdot \boldsymbol{u}_1 d\hat{x} + \frac{F_{y1}}{A_1}\int_0^1 K_F^{-1}\boldsymbol{v}_1 \cdot \boldsymbol{u}_1 d\hat{x} \\ &=\; \frac{(F_{x0}+F_{x1})\|\boldsymbol{u}_1\|}{2K_F\|\boldsymbol{v}_1\|} . \end{aligned} \tag{35}$$

6. ACKNOWLEDGMENTS

This work was supported by the International Research Training Group "Non-Linearities and Upscaling in Porous Media (NUPUS)" financed by the German Research Foundation (DFG) and in parts by the Norwegian Research Council, StatoilHydro, and Norske Shell under grant no. 178013/13. The authors would like to thank Jan Nordbotten for useful suggestions and discussion regarding the flux recovery procedure.

References

[1] Al-Huthali, A., and A. Datta-Gupta, Streamline simulation of counter-current imbibition in naturally fractured reservoir, *J. Petrol. Sci. Eng., 43(3-4)*, 271-300, 2004.

[2] Assteerawatt, A., *Flow and Transport Modelling of Fractured Aquifers based on a Geostatistical Approach*, (http://elib.uni-stuttgart.de/opus/volltexte/2008/3639/), PhD Thesis, Universität Stuttgart, Institute of Hydraulic Engineering, 2008.

[3] Assteerawatt, A., H. Hægland, R. Helmig, A. Bárdossy and H. K. Dahle, Simulation of flow and transport processes in a discrete fracture-matrix system I. geostatistical generation of fractures on an aquifer analogue scale, *Water Resour. Res.*, submitted.

[4] Bear, J., *Dynamics of Fluids in Porous Media*, Academic Press, California, 1972.

[5] Cockburn, B., J. Gopalakrishnan, and H. Wang, Locally conservative fluxes for the continuous Galerkin method, *SIAM J. Numer. Anal., 45(4)*, 1742-1776, 2007.

[6] Cordes, C., and W. Kinzelbach, Continuous groundwater velocity fields and path lines in linear, bilinear, and trilinear finite elements, *Water Resour. Res., 28(11)*, 2903-2911, 1992.

[7] Correa, M.R., and A.F.D. Loula., Stabilized velocity post-processing for Darcy flow in heterogeneous porous media, *Commun. Numer. Meth. En., 23*, 461-489, 2007.

[8] Durlofsky, L.J., Accuracy of mixed and control volume finite element approximations to Darcy velocity and related quantities, *Water Resour. Res., 30(4)*, 965-973, 1994.

[9] Hægland, H., Streamline tracing on irregular grids (http://www.mi.uib.no/~hakonh/thesis/thesis.pdf), *Master's thesis, University of Bergen, Dept. of Mathematics*, 2003.

[10] Hægland, H., A. Assteerawatt, H. Dahle, G.T. Eigestad, and R. Helmig, Comparison of cell- and vertex centered discretization methods for flow in a discrete fracture-matrix system, in preparation.

[11] Hægland, H., H.K. Dahle, G.T. Eigestad, K.-A. Lie, and I. Aavatsmark, Improved streamlines and time-of-flight for streamline simulation on irregular grids, *Adv. Water Resour., 30(4)*, 1027-1045, 2007.

[12] Huang, W., G.D. Donato, and M.J. Blunt, Comparison of streamline-based and grid-based dual porosity simulation, *J. Petrol. Sci. Eng., 43(1-2)*, 129-137, 2004.

[13] Jimenez, E., K. Sabir, A. Datta-Gupta, and M.J. King, Spatial error and convergence in streamline simulation, *SPE Reserv. Eval. Eng., 10(3)*, 221-232, June 2007.

[14] Karimi-Fard, M., L.J. Durlofsky, and K. Aziz, An efficient discrete fracture model applicable for general purpose reservoir simulators, *SPE J.*, 227-236, June 2004.

[15] King, M.J., and A. Datta-Gupta, Streamline simulation: A current perspective, *In Situ, 22(1)*, 91-140, 1998.

[16] Lee, S.H., M.F. Lough, and C.L. Jensen Hierarchical modeling of flow in naturally fractured formations with multiple length scales, *Water Resour. Res., 37(3)*, 443-455, 2001.

[17] Ma, J., G.D. Couples, and S.D. Harris, A mixed finite element technique based on implicit discretization of faults for permeability upscaling in fault damage zones, *Water Resour. Res., 42*, W08413, doi:10.1029/2005WR004686, 2006.

[18] Matringe, S.F., R. Juanes and H.A. Tchelepi, Robust streamline tracing for the simulation of porous media flow on general triangular and quadrilateral grids, *J. Comput. Phys., 219(2)*, doi:10.1016/j.jcp.2006.07.004, 2006.

[19] Neunhäuserer, L., *Diskretisierungsansätze zur Modellierung von Strömungs- und Transportprozessen in geklüftet-porösen Medien* (http://elib.uni-stuttgart.de/opus/volltexte/2003/1477/), PhD Thesis, Universität Stuttgart, Institute of Hydraulic Engineering, 2003.

[20] Pollock, D.W., Semi-analytical computation of path lines for finite-difference models, *Ground Water, 26(6)*, 743-750, 1988.

[21] Prévost, M. *Accurate coarse reservoir modeling using unstructured grids, flow-based upscaling and streamline simulation* (http://geothermal.standford.edu/pereposts/search.htm), PhD Thesis, University of Standford, 2003.

[22] Prévost, M., M.G. Edwards, and M.J. Blunt, Streamline tracing on curvilinear structured and unstructured grids, *SPE J.*, 139-148, June 2002.

[23] Reichenberger, V., H. Jakobs, P. Bastian, and R. Helmig, A mixed-dimensional finite volume method for two-phase flow in fractured porous media, *Adv. Water Resour., 29(7)*, 1020-1036, 2006.

[24] Silberhorn-Hemminger, A., *Modellierung von Kluftaquifersystemen: Geostatistische analyse und deterministisch – stochastische Kluftgenerierung* (http://elib.uni-stuttgart.de/opus/volltexte/2003/1278/), PhD Thesis, Universität Stuttgart, Institute of Hydraulic Engineering, 2002.

[25] Srivastava, R., and M.L. Brusseau, Darcy velocity computations in the finite element method for multidimensional randomly heterogeneous porous media, *Adv. Water Resour., 18(4)*, 191-201, 1995.
[26] Sun, S., and M.F. Wheeler, Projections of velocity data for the compatibility with transport, *Comput. Methods Appl. Mech. Engrg., 195*, 653-673, 2006.
[27] Thiele, M.R., Streamline simulation, In *P*roceedings of the 8th International Forum on Reservoir Simulation, Stresa / Lago Maggiore, Italy, 2005.